nature geoscience

ARTICLES

https://doi.org/10.1038/s41561-022-00908-3

Check for updates

Instability of the African large low-shear-wave-velocity province due to its low intrinsic density

Qian Yuan ✉ and Mingming Li

Seismic observations have revealed two seismic anomalies in the lowermost mantle, one beneath Africa and the other beneath the Pacific Ocean, named large low-shear-wave-velocity provinces. These structures are generally considered to be intrinsically dense thermochemical piles that influence mantle and core processes. However, the controls on their morphology, including their relative height difference and their stability, remain unclear. Here we analyse published global shear-wave tomography models, which show that the African anomaly is about 1,000 km greater in height than the Pacific anomaly. With our numerical simulations, we find that the maximum height a thermochemical pile can reach is more controlled by its density and the surrounding mantle viscosity, and less so by its own viscosity and volume. Comparing these findings suggests that the African anomaly has a relatively lower density and thus may be less stable than the Pacific anomaly, implying the two anomalies have different compositions, dynamics and evolution histories.

Understanding Earth's deep mantle structure, dynamics and evolution remains one of the most challenging and important tasks in solid Earth sciences. Seismic observations have revealed two large low-shear-velocity provinces (LLSVPs, Fig. 1) in the lowermost mantle beneath Africa and the Pacific Ocean[1–4]. The LLSVPs are the largest contiguous structures in Earth's mantle and they considerably impact surface volcanism, deep mantle convection and core heat flux that is responsible for dynamo[5,6]. However, it remains unclear what causes the LLSVPs and how they interact with the surrounding mantle. Deciphering the origin and dynamics of the LLSVPs requires a better understanding of the physical properties of the LLSVPs, particularly their density and viscosity differences with the surrounding mantle. However, deep mantle density and viscosity are not well resolved, which inhibits fully comprehending the origin and dynamics of LLSVPs. Importantly, the morphology of the LLSVPs is an expression of their interaction with the surrounding mantle dynamics, which is controlled by and thus provides information on the deep mantle density and viscosity structures.

Height difference between the two LLSVPs

The morphology of the LLSVPs has been investigated through seismic observations[7–11]. Seismic waveform modelling studies have suggested that the African LLSVP reaches a height of ~1,300–1,500 km above the core–mantle boundary (CMB)[11,12], whereas the Pacific LLSVP reaches a lower height of ~500–800 km (ref. [8]). However, the results of seismic forward waveform modelling can contain trade-offs between the size of structures and their seismic velocities[13]. Also, the sizes of LLSVPs imaged in global tomography have been previously defined in regions where the shear-wave seismic velocity anomaly (dV_s) is lower than a chosen threshold, but the results can vary significantly with the selected threshold[7,14].

Here we use an approach to complement previous studies to estimate the maximum height of the LLSVPs. We select 17 global shear-wave tomography models[2,15–30], and for each model, we calculate the lateral average dV_s (denoted as $\overline{dV_s}$) as a function of the height (H) above the CMB in vertical cross sections that cut through the LLSVP regions (Fig. 1a and Extended Data Fig. 1). We compute the $\overline{dV_s}$-H profile for all 17 models and calculate their average (Fig. 1b,c). It is found that the lower mantle $\overline{dV_s}$ is most negative near the CMB and increases linearly with H until a turning point (for example, grey regions in Fig. 1b,c) where the gradient, as shown in Extended Data Figs. 2 and 3, changes from mostly positive to zero or negative. The increase of the $\overline{dV_s}$ with H below the turning point may be caused by LLSVPs having a wider base (at smaller H) than the top (at larger H). The turning point may therefore mark the transition from depths with LLSVPs to depths without LLSVPs and thus represents the maximum height of LLSVPs. We examined 33 vertical cross sections through the LLSVPs (Extended Data Figs. 4 and 5) and found four cross sections showing the maximum heights of the LLSVPs. With this approach, the maximum height estimated is ~700–800 km for the Pacific LLSVP and ~1,600–1,800 km for the African LLSVP (Fig. 1b,c), which is consistent with regional waveform modelling[8,11,12]. To account for the difference of dV_s magnitude in different tomography models, we normalized the dV_s of each vertical cross section in each tomography model by the maximum magnitude of the dV_s in the cross section before calculating the $\overline{dV_s}$-H profiles, and the results (Supplementary Figs. 1 and 2) confirm the heights of the two LLSVPs defined in Fig. 1b,c. Cottaar and Lekic[7] performed cluster analysis of tomography models and defined the LLSVP domains in seismically 'slow' regions. Using the same definition of the LLSVP domains, we compute the area of each LLSVP as a function of depth and find that the depths with the largest changes of the LLSVP areas are broadly consistent with the LLSVP heights in Fig. 1b,c (Supplementary Fig. 3), which further supports the large height difference between the two LLSVPs.

The question remains as to what causes the large height difference between the two LLSVPs. The LLSVPs have been hypothesized to be caused by compositionally distinct materials that are intrinsically denser than the surrounding mantle[31–34], although other possible origins of the LLSVPs, such as purely thermal structures[35,36] and clusters of slow anomalies[37,38], have not been ruled out. Previous numerical modelling and laboratory experiments have shown that the height of a thermochemical pile is greatly controlled by its density and viscosity compared to that of the surrounding mantle[32,39–43]. However, it remains unclear through what

School of Earth and Space Exploration, Arizona State University, Tempe, AZ, USA. ✉e-mail: qyuan23@asu.edu

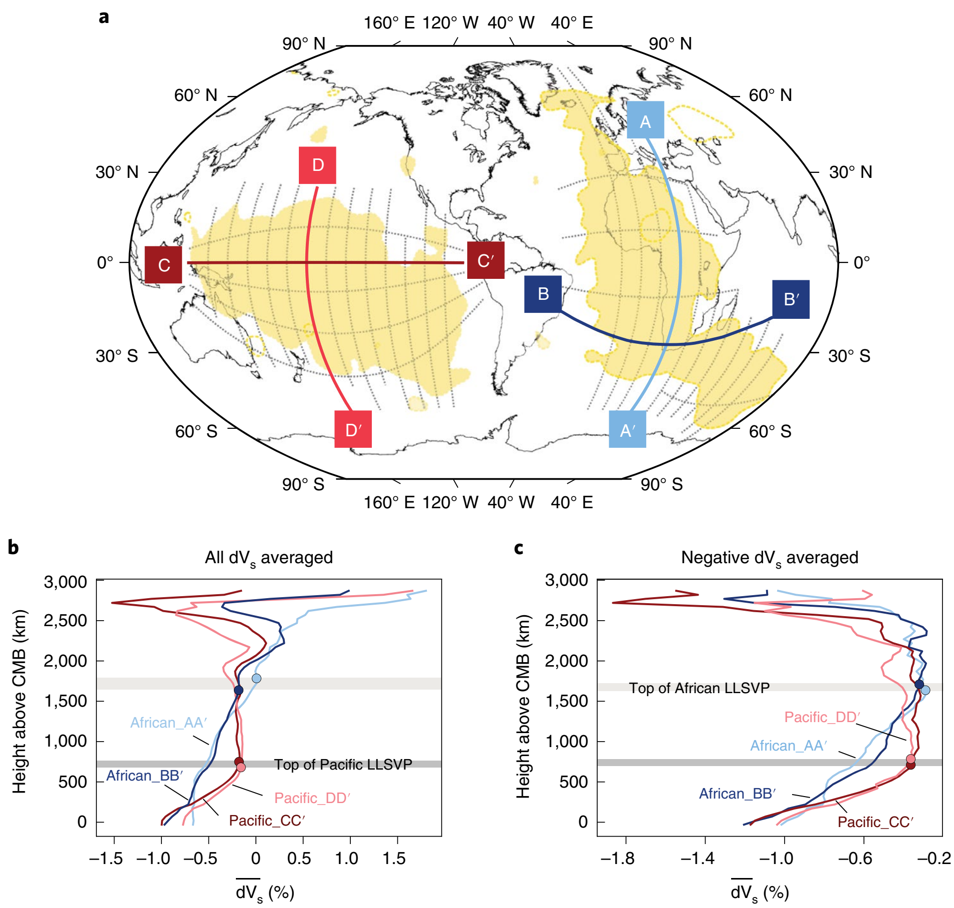

Fig. 1 | Depth profiles of the lateral average shear-wave velocity anomaly ($\overline{dV_s}$) at four vertical cross-sectional locations through the LLSVPs. **a**, Locations of four vertical cross sections (thick, solid lines) on two LLSVPs (yellow, from ref. [29]), from which $\overline{dV_s}$ is computed as a function of height (H) above the CMB. **b**, The averaged $\overline{dV_s}$-H profiles from 17 tomography models. **c**, Same as **b** except only the negative dV_s is used to calculate $\overline{dV_s}$. Circles in **b** and **c** show turning points where the gradients of $\overline{dV_s}$-H profiles change from mostly positive to zero or negative (Extended Data Figs. 2 and 3). The two horizontal grey bars in **b** and **c** indicate the height ranges of two LLSVPs bounded by the turning points. Figure 1a was generated using GMT software version 6.0.0 (https://www.generic-mapping-tools.org/).

mechanism these properties control the height of a pile and how to explain the vast height difference between the two LLSVPs.

Controls on the height of thermochemical piles

Here we perform geodynamic modelling experiments to quantify the relationship between the height of thermochemical piles and the density and viscosity structure of the mantle. The conservation equations are solved under the Boussinesq approximation with the Citcom code in 2D Cartesian geometry[44]. Most models have an aspect ratio of 1:1 and some have a 6:1 aspect ratio. The models contain two compositional components: pile material and background mantle material. The intrinsic density anomaly of pile materials with respect to background mantle material is represented by the buoyancy number (B), and the intrinsic density anomaly of an element in the model domain is calculated by the product of B and the fraction of pile materials within the element, which is defined as the effective buoyancy ratio, or B^{eff} (Methods). The reference values used here are listed in Supplementary Table 1. The viscosity depends on composition, but temperature-dependent viscosity is also employed in some cases. The Rayleigh number (Ra) is 1×10^6 for all cases, but mantle viscosity varies in each case, which leads to a wide range of effective Rayleigh numbers and vigour of convection. Supplementary Data 1 lists the parameters for all models used in this study. Additional details about model setup are in the Methods section.

Shortly after initial condition, the pile materials are pushed into a thermochemical pile (for example, Fig. 2a–c). We define the height of a thermochemical pile as the vertical distance from the bottom of the model to the depth location above the CMB where the lateral extent of the pile drops below 5% of the lateral extent of the pile at the bottom (Fig. 2d–l). We measure the pile height for each timestep during a time window when the model statistically reaches quasi-steady state. Then, we calculate the average and the standard deviation of the pile height during this period.

We define a reference case with a buoyancy number of 0.8 and a viscosity of 2×10^{20} Pa s for the pile materials that initially occupy the lowermost 7% of the model domain and a background mantle viscosity of 2×10^{22} Pa s. We first show the effect of initial volume of pile materials on the height of the pile. We vary the initial pile volume from 3% to 11% of the model domain and find that the pile height is not significantly affected by the volume of pile materials (Figs. 2a–f and 3a). Adding more pile material to the model domain increases only the lateral extent of the pile but not its vertical elevation (Fig. 2d–f). We do not consider cases in which the pile material occupies more than 11% of the model domain, because a global layer of pile material forms in these cases that is inconsistent with the LLSVPs that are spatially isolated. In models where the initial volume of pile material is less than 3% of the model domain and other parameters are kept the same as

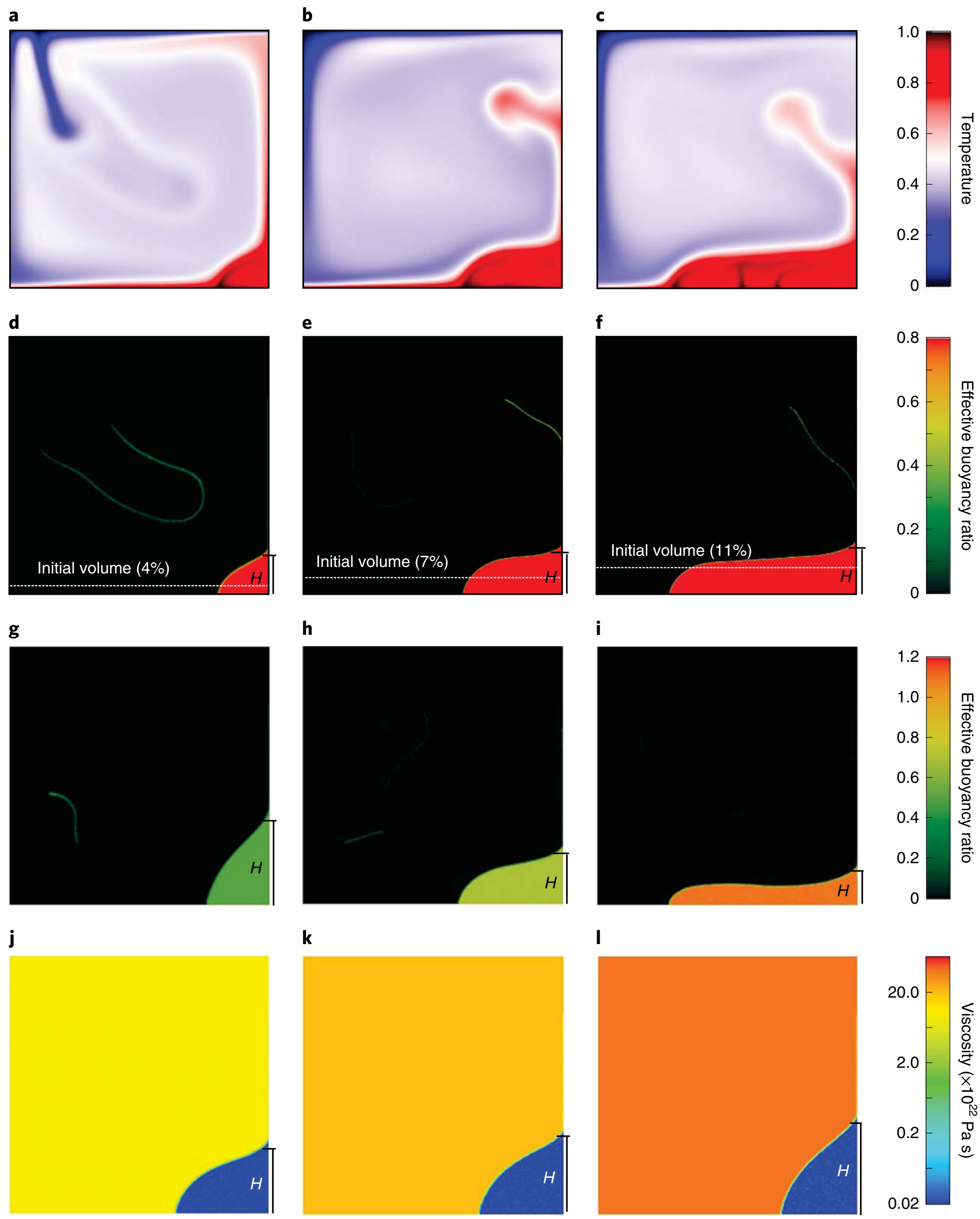

Fig. 2 | The effects of volume and buoyancy number of pile materials and background mantle viscosity on the height of piles. a–l, Snapshots of temperature (**a**–**c**), composition, represented by effective buoyancy ratio (**d**–**i**), and viscosity (**j**–**l**) fields in cases where pile volume is 4% (**a**,**d**), 7% (**b**,**e**) and 11% (**c**,**f**) of model domain; pile buoyancy number is 0.5 (**g**), 0.7 (**h**) and 1.1 (**i**); and background mantle viscosity is 1×10^{23} Pa s (**j**), 2×10^{23} Pa s (**k**) and 4×10^{23} Pa s (**l**). The temperature (**a**–**c**) and composition (**d**–**i**) are dimensionless values. White lines in **d**–**f** show initial pile heights. *H* in **d**–**l** shows final pile height.

the reference case, the pile is quickly entrained into the ambient mantle, even when we double the model resolution. A pile with a volume much less than ~3% of the model domain could have a much lower height than larger piles[45] and could be stable if they also have high intrinsic density (such as the compositionally distinct ultra-low velocity zones[46]), but the volume of the pile is not comparable to the LLSVPs, which have been estimated to be as large as 8% of mantle volume[7].

We investigate the effects of buoyancy number B on the pile height. We find that when B is smaller than 0.45, the pile material becomes unstable and is mixed into the background mantle quickly, and when B is larger than 1.25, the pile material forms a stable global layer at the bottom. Snapshots of three cases with B of 0.5, 0.7 and 1.1 are shown in Fig. 2g–i, and Fig. 3b shows the pile height for 16 cases with B from 0.5 to 1.25. As expected, the pile height decreases substantially with increases of B.

We investigate the influence of background mantle viscosity (η_{bg}) on the height of the pile. We vary η_{bg} in 26 cases from 2×10^{22} Pa s to 5×10^{23} Pa s and keep other parameters the same as the reference case. We find that the height of the pile increases with η_{bg} (Figs. 2j–l and 3c). However, the influence of η_{bg} on pile height becomes weak when η_{bg} is larger than ~10×10^{22} Pa s (Fig. 3c).

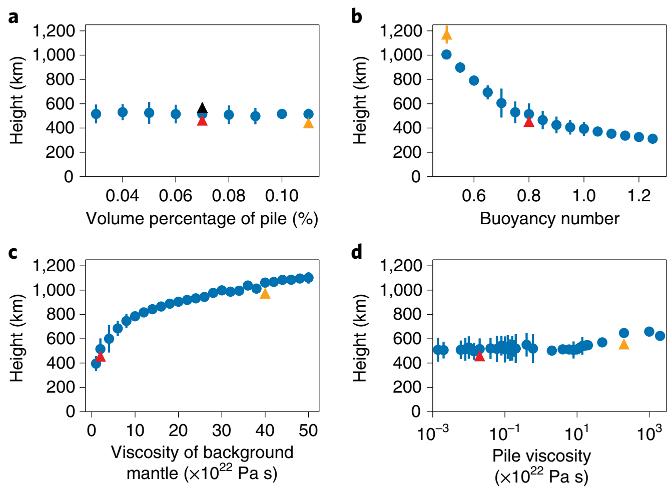

Fig. 3 | Effects of model parameters on the height of piles. a–d, Parameters include pile volume (**a**), buoyancy number (**b**), background mantle viscosity (**c**) and pile viscosity (**d**). Each blue dot shows the average pile height in a 2D model under statistically steady state with error bars showing the standard deviation. Orange triangles show pile heights in 3D models with same parameters as their corresponding 2D models. Red and black triangles represent the reference 3D model with black triangle for higher resolution. Reference 2D and 3D models use a buoyancy number of 0.8 and a viscosity of 2×10^{20} Pa s for pile materials.

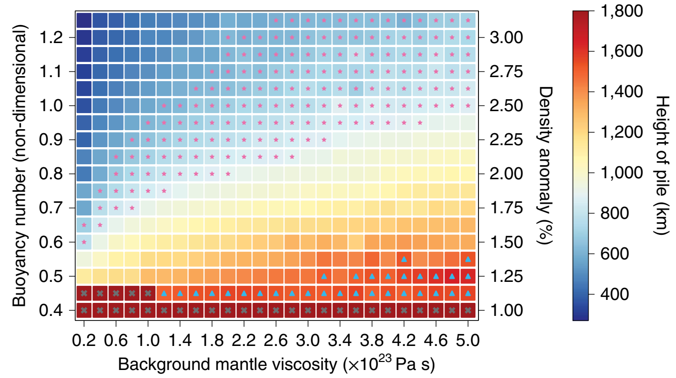

Fig. 4 | The height of piles as a function of pile buoyancy number and background mantle viscosity. Pink stars (blue triangles) show cases in which the heights of piles are 600–900 km (1,500–1,900 km), which are comparable to the heights of the Pacific (African) LLSVP of 700–800 km (1,600–1,800 km) after considering that the heights of piles have an uncertainty of ~100 km. Grey crosses show cases in which thermochemical piles are not stable.

We also explore how the viscosity of pile material affects pile height. We vary the pile viscosity from 1.4×10^{19} Pa s to 2×10^{25} Pa s in 32 cases and keep other parameters the same as the reference case. We find that the height of the pile in these cases is similar to the reference case and we observe a moderate increase of pile height (by up to 150 km) when the pile viscosity is at least hundreds of times higher than the background mantle (Fig. 3d).

The results shown above demonstrate that the height of a stable thermochemical pile is much more controlled by the background mantle viscosity and the buoyancy number of the pile material than the pile viscosity and pile volume in the range of 3–11% of model domain. These results are consistent with previous studies showing pile height scales with Ra by $\mathrm{Ra}^{-1/3}$ (proportional to the reference mantle viscosity)[32,42] and with the buoyancy number by $B^{-0.5}$ (ref. [41]). As shown in Extended Data Figs. 6 and 7, a smaller B leads to larger residual buoyancy of piles, making the piles easier to be pushed up by convection currents, and a higher η_{bg} leads to larger deviatoric stresses at the pile margins, which may cause larger pile height. However, the pile viscosity and volume neither affect the pile buoyancy nor the deviatoric stresses applied to the pile margins from outside, which may explain why they do not considerably affect the pile height.

We next show the pile height for different combinations of pile B and η_{bg}. We systematically vary the B from 0.4 to 1.25 and the η_{bg} from 2×10^{22} Pa s to 5×10^{23} Pa s, and 450 individual models are run for different combinations of the two parameters (Supplementary Data 1). To avoid the influence of the minor mantle temperature differences between different models, we also perform a reference case and allow the temperature field to reach quasi-steady state after which we restart the case but change the B and η_{bg}. This gives us another 450 models (defined here as re-run models, Supplementary Data 1). We compute the pile height when it reaches a new quasi-steady state but before there are any noticeable temperature changes (>95% similarity, Supplementary Data 1) in the mantle. This approach allows all the re-run models to have nearly the same temperature-controlled part of the buoyancy fields.

Figure 4 shows pile height as a function of B and η_{bg} for the 450 re-run models, which shows results nearly the same as the individual models (Extended Data Fig. 8). The pink stars (blue triangles) mark cases in which the pile heights are comparable to the height of the Pacific (African) LLSVP. We find that the height of the Pacific LLSVP can be explained by a wide range of B and η_{bg}, and there is a clear trade-off between the two parameters. However, the height of the African LLSVP can be explained only by B in a narrow range of 0.45–0.55. For B of 0.55, the η_{bg} required to explain the African LLSVP height is more than 4×10^{23} Pa s, which is unrealistically high[47,48]. Piles can become taller as B further decreases; however, for B lower than 0.45, piles become less stable (grey crosses in Fig. 4) with more than half of their volume mixed into the background mantle after ~4.6 Gyr.

Effects of additional model complexities

We test cases with an aspect ratio of 6:1 and find that effects of the aspect ratio on pile heights are very minor (Extended Data Fig. 9). Cases with temperature-dependent viscosity are also performed (Supplementary Data 1), in which the η_{bg} near the pile margins is greatly reduced due to the increase of temperature, and as a result, the pile height is reduced. We find that the viscosity in regions close to the pile edges plays a controlling role for the pile height (Supplementary Fig. 4), which is consistent with previous laboratory experiments[43,49,50]. The η_{bg} near pile margins and the pile height would further decrease with a more strongly temperature-dependent viscosity (Supplementary Fig. 4), making it more difficult to explain the large African LLSVP height. We also perform six 3D models in spherical geometry with different initial pile volume, pile viscosity, pile B, η_{bg} and model resolution. The setup of 3D models is described in the Methods section. Except the difference of geometry, the model parameters are kept the same as the corresponding 2D models. We find that the pile heights in 3D models are similar to their corresponding 2D models (Fig. 3 and Extended Data Fig. 10). Adding more model complexities such as spin transition in the lower mantle[51] and compositional dependence of compressibility[52] would affect the pile height, but may not explain the large (~1,000 km) height difference between the two LLSVPs because they would affect the heights of both LLSVPs in a similar way.

One possibility is that the seismically observed LLSVPs may contain an inner domain of thermochemical piles and an outer domain of purely thermal structures and thus the measured LLSVP heights defined in Fig. 1 are larger than that of the thermochemical piles. The purely thermal parts of LLSVPs could be caused by a thermal boundary layer around the margins of thermochemical piles or thermal mantle plumes. However, the thickness of the thermal boundary layer may be small (for example, less than ~100 km, Fig. 2a–f), and mantle plumes probably occur on both LLSVPs. Therefore, under this possibility, it remains difficult to explain the large height difference for the two LLSVPs. In addition, seismic observations by Simmons et al.[53] showed that the thermochemical section of the African LLSVP reaches more than 1,500 km above the CMB, but there is no such evidence for the Pacific LLSVP.

We here focus on quasi-steady state features of piles. If the Earth's mantle dynamics are not close to a steady state, it is plausible that the heights of LLSVPs are changing, perhaps differently, over time. The uplift history during the Oligocene in the African continent may support this idea[54]. Davaille[39] found that piles can oscillate between phases of rising and collapse, which may explain different heights of two LLSVPs if they are in different phases of oscillation. However, in their experiments, the pile materials cover more than half the depth of a tank, and a continuous global layer always covers the bottom of the tank during the oscillatory process, which is different from the seismically imaged LLSVPs (which are spatially isolated). It remains unclear if such oscillatory behaviour still occurs if the volume of pile materials is comparable to that of LLSVPs. Nevertheless, the piles oscillating up and down in the tank experiments are unstable structures, which is in line with our interpretation that the African LLSVP may be unstable, although our results do not rule out the possibility that the Pacific LLSVP may be unstable as well.

Implications for distinct LLSVP compositions and evolution histories

To summarize, the ~1,000 km larger height of the African LLSVP compared with the Pacific LLSVP indicates that at least the African LLSVP is unstable, and the vast height difference implies that the two LLSVPs may have different densities and thus different compositions. The compositional difference between the LLSVPs is corroborated by a recent study of radiogenic isotopes (lead, neodymium and strontium) on plume-induced basalts above LLSVPs, showing the African LLSVP is enriched by less dense subducted upper continental materials during the Pangaea supercontinent cycle but no such feature in the Pacific LLSVP[55]. The compositional difference of the LLSVPs may be caused by their different long-term interactions that lead to a different amount of material exchange with the surrounding mantle. Our results thus imply different evolution and dynamics of the two LLSVPs.

Online content

Any methods, additional references, Nature Research reporting summaries, source data, extended data, supplementary information, acknowledgements, peer review information; details of author contributions and competing interests; and statements of data and code availability are available at https://doi.org/10.1038/s41561-022-00908-3.

Received: 13 August 2020; Accepted: 31 January 2022;
Published online: 10 March 2022

References

1. Garnero, E. J., McNamara, A. K. & Shim, S. H. Continent-sized anomalous zones with low seismic velocity at the base of Earth's mantle. *Nat. Geosci.* **9**, 481–489 (2016).
2. Grand, S. P. Mantle shear-wave tomography and the fate of subducted slabs. *Philos. Trans. R. Soc. A* **360**, 2475–2491 (2002).
3. Li, X.-D. & Romanowicz, B. Global mantle shear velocity model developed using nonlinear asymptotic coupling theory. *J. Geophys. Res. Solid Earth* **101**, 22245–22272 (1996).
4. Ritsema, J., van Heijst, H. J. & Woodhouse, J. H. Global transition zone tomography. *J. Geophys. Res.* **109**, B02302 (2004).
5. Li, M., Zhong, S. & Olson, P. Linking lowermost mantle structure, core–mantle boundary heat flux and mantle plume formation. *Phys. Earth Planet. Inter.* **277**, 10–29 (2018).
6. Olson, P. & Amit, H. Magnetic reversal frequency scaling in dynamos with thermochemical convection. *Phys. Earth Planet. Inter.* **229**, 122–133 (2014).
7. Cottaar, S. & Lekic, V. Morphology of seismically slow lower-mantle structures. *Geophys. J. Int.* **207**, 1122–1136 (2016).
8. He, Y. & Wen, L. Structural features and shear-velocity structure of the 'Pacific Anomaly'. *J. Geophys. Res. Solid Earth* **114**, B02309 (2009).
9. Lekic, V., Cottaar, S., Dziewonski, A. & Romanowicz, B. Cluster analysis of global lower mantle tomography: a new class of structure and implications for chemical heterogeneity. *Earth Planet. Sci. Lett.* **357–358**, 68–77 (2012).
10. Ni, S. & Helmberger, D. V. Ridge-like lower mantle structure beneath South Africa. *J. Geophys. Res.* **108**, 2094 (2003).
11. Wang, Y. & Wen, L. Geometry and P and S velocity structure of the 'African Anomaly'. *J. Geophys. Res. Solid Earth* **112**, B05313 (2007).
12. Ni, S., Tan, E., Gurnis, M. & Helmberger, D. Sharp sides to the African superplume. *Science* **296**, 1850–1852 (2002).
13. Rawlinson, N., Fichtner, A., Sambridge, M. & Young, M. K. in *Advances in Geophysics,* Vol. 55 (ed Dmowska, R.) Ch. 1 (Elsevier, 2014).
14. Burke, K., Steinberger, B., Torsvik, T. H. & Smethurst, M. A. Plume generation zones at the margins of large low shear velocity provinces on the core–mantle boundary. *Earth Planet. Sci. Lett.* **265**, 49–60 (2008).
15. Simmons, N. A., Forte, A. M., Boschi, L. & Grand, S. P. GyPSuM: a joint tomographic model of mantle density and seismic wave speeds. *J. Geophys. Res. Solid Earth* **115**, B12310 (2010).
16. Panning, M. P., Lekić, V. & Romanowicz, B. A. Importance of crustal corrections in the development of a new global model of radial anisotropy. *J. Geophys. Res. Solid Earth* **115**, B12325 (2010).
17. French, S. W. & Romanowicz, B. A. Whole-mantle radially anisotropic shear velocity structure from spectral-element waveform tomography. *Geophys. J. Int.* **199**, 1303–1327 (2014).
18. Lekić, V. & Romanowicz, B. Inferring upper-mantle structure by full waveform tomography with the spectral element method. *Geophys. J. Int.* **185**, 799–831 (2011).
19. Chang, S. J., Ferreira, A. M. G., Ritsema, J., van Heijst, H. J. & Woodhouse, J. H. Joint inversion for global isotropic and radially anisotropic mantle structure including crustal thickness perturbations. *J. Geophys. Res. Solid Earth* **120**, 4278–4300 (2015).
20. Lu, C. & Grand, S. P. The effect of subducting slabs in global shear wave tomography. *Geophys. J. Int.* **205**, 1074–1085 (2016).
21. Durand, S., Debayle, E., Ricard, Y. & Lambotte, S. Seismic evidence for a change in the large-scale tomographic pattern across the D′′ layer. *Geophys. Res. Lett.* **43**, 7928–7936 (2016).
22. Durand, S., Debayle, E., Ricard, Y., Zaroli, C. & Lambotte, S. Confirmation of a change in the global shear velocity pattern at around 1,000 km depth. *Geophys. J. Int.* **211**, 1628–1639 (2017).
23. Houser, C., Masters, G., Shearer, P. & Laske, G. Shear and compressional velocity models of the mantle from cluster analysis of long-period waveforms. *Geophys. J. Int.* **174**, 195–212 (2008).
24. Montelli, R., Nolet, G., Dahlen, F. A. & Masters, G. A catalogue of deep mantle plumes: new results from finite-frequency tomography. *Geochem. Geophys. Geosyst.* **7**, Q11007 (2006).
25. Koelemeijer, P., Ritsema, J., Deuss, A. & van Heijst, H. J. SP12RTS: a degree-12 model of shear- and compressional-wave velocity for Earth's mantle. *Geophys. J. Int.* **204**, 1024–1039 (2016).
26. Tesoniero, A., Auer, L., Boschi, L. & Cammarano, F. Hydration of marginal basins and compositional variations within the continental lithospheric mantle inferred from a new global model of shear and compressional velocity. *J. Geophys. Res. Solid Earth* **120**, 7789–7813 (2015).
27. Ritsema, J., van Heijst, H. J. & Woodhouse, J. H. Complex shear wave velocity structure imaged beneath Africa and Iceland. *Science* **286**, 1925–1931 (1999).
28. Moulik, P. & Ekström, G. An anisotropic shear velocity model of the Earth's mantle using normal modes, body waves, surface waves and long-period waveforms. *Geophys. J. Int.* **199**, 1713–1738 (2014).
29. Ritsema, J., Deuss, A., van Heijst, H. J. & Woodhouse, J. H. S40RTS: a degree-40 shear-velocity model for the mantle from new Rayleigh wave dispersion, teleseismic traveltime and normal-mode splitting function measurements. *Geophys. J. Int.* **184**, 1223–1236 (2011).
30. Auer, L., Boschi, L., Becker, T. W. & Giardini, D. Savani: a variable resolution whole-mantle model of anisotropic shear velocity variations based on multiple data sets. *J. Geophys. Res. Solid Earth* **119**, 3006–3034 (2014).
31. Li, M. & Zhong, S. The source location of mantle plumes from 3D spherical models of mantle convection. *Earth Planet. Sci. Lett.* **478**, 47–57 (2017).
32. Tackley, P. J. in *The Core–Mantle Boundary Region* Vol. 28 (eds Gurnis, M. et al.) 231–253 (American Geophysical Union, 1998).

33. McNamara, A. K. & Zhong, S. Thermochemical structures beneath Africa and the Pacific Ocean. *Nature* **437**, 1136–1139 (2005).
34. Zhang, N., Zhong, S., Leng, W. & Li, Z. X. A model for the evolution of the Earth's mantle structure since the Early Paleozoic. *J. Geophys. Res. Solid Earth* **115**, B06401 (2010).
35. Bull, A. L., McNamara, A. K. & Ritsema, J. Synthetic tomography of plume clusters and thermochemical piles. *Earth Planet. Sci. Lett.* **278**, 152–162 (2009).
36. Davies, D. R. et al. Reconciling dynamic and seismic models of Earth's lower mantle: the dominant role of thermal heterogeneity. *Earth Planet. Sci. Lett.* **353–354**, 253–269 (2012).
37. Davaille, A. & Romanowicz, B. Deflating the LLSVPs: bundles of mantle thermochemical plumes rather than thick stagnant "piles". *Tectonics* **39**, e2020TC006265 (2020).
38. Hosseini, K. et al. Global mantle structure from multifrequency tomography using P, PP and P-diffracted waves. *Geophys. J. Int.* **220**, 96–141 (2020).
39. Davaille, A. Simultaneous generation of hotspots and superwells by convection in a heterogeneous planetary mantle. *Nature* **402**, 756–760 (1999).
40. Davaille, A., Le Bars, M. & Carbonne, C. Thermal convection in a heterogeneous mantle. Convection thermique dans un manteau hétérogène. *C. R. Geosci.* **335**, 141–156 (2003).
41. Jellinek, A. M. & Manga, M. Links between long-lived hot spots, mantle plumes, D″, and plate tectonics. *Rev. Geophys.* **42**, RG3002 (2004).
42. Kumagai, I., Davaille, A. & Kurita, K. On the fate of thermally buoyant mantle plumes at density interfaces. *Earth Planet. Sci. Lett.* **254**, 180–193 (2007).
43. Le Bars, M. & Davaille, A. Whole layer convection in a heterogeneous planetary mantle. *J. Geophys. Res.* **109**, B03403 (2004).
44. Moresi, L. N. & Solomatov, V. S. Numerical investigation of 2D convection with extremely large viscosity variations. *Phys. Fluids* **7**, 2154–2162 (1995).
45. Langemeyer, S. M., Lowman, J. P. & Tackley, P. J. The dynamics and impact of compositionally originating provinces in a mantle convection model featuring rheologically obtained plates. *Geophys. J. Int.* **220**, 1700–1716 (2020).
46. Li, M., McNamara, A. K., Garnero, E. J. & Yu, S. Compositionally-distinct ultra-low velocity zones on Earth's core–mantle boundary. *Nat. Commun.* **8**, 177 (2017).
47. Mitrovica, J. X. & Forte, A. M. A new inference of mantle viscosity based upon joint inversion of convection and glacial isostatic adjustment data. *Earth Planet. Sci. Lett.* **225**, 177–189 (2004).
48. Steinberger, B. & Calderwood, A. R. Models of large-scale viscous flow in the Earth's mantle with constraints from mineral physics and surface observations. *Geophys. J. Int.* **167**, 1461–1481 (2006).
49. Davaille, A. & Jaupart, C. Transient high-Rayleigh-number thermal convection with large viscosity variations. *J. Fluid Mech.* **253**, 141–166 (1993).
50. Le Bars, M. & Davaille, A. Large interface deformation in two-layer thermal convection of miscible viscous fluids. *J. Fluid Mech.* **499**, 75–110 (2004).
51. Huang, C., Leng, W. & Wu, Z. Iron-spin transition controls structure and stability of LLSVPs in the lower mantle. *Earth Planet. Sci. Lett.* **423**, 173–181 (2015).
52. Tan, E. & Gurnis, M. Metastable superplumes and mantle compressibility. *Geophys. Res. Lett.* **32**, L20307 (2005).
53. Simmons, N. A., Forte, A. M. & Grand, S. P. Thermochemical structure and dynamics of the African superplume. *Geophys. Res. Lett.* **34**, L02301 (2007).
54. Burke, K. & Gunnell, Y. *The African Erosion Surface: A Continental-Scale Synthesis of Geomorphology, Tectonics, and Environmental Change Over the Past 180 Million Years* (Geological Society of America, 2008).
55. Doucet, L. S. et al. Distinct formation history for deep-mantle domains reflected in geochemical differences. *Nat. Geosci.* **13**, 511–515 (2020).

Publisher's note Springer Nature remains neutral with regard to jurisdictional claims in published maps and institutional affiliations.

Methods

Governing equations. We perform geodynamic calculations by solving the following non-dimensional equations of conservation of mass, momentum and energy under the Boussinesq approximation:

$$\nabla \cdot \vec{\mathbf{u}} = 0 \quad (1)$$

$$-\nabla P + \nabla \cdot (\eta \epsilon) = \mathrm{Ra}\,(T - BC)\,\vec{\mathbf{z}} \quad (2)$$

$$\frac{\partial T}{\partial t} + (\vec{\mathbf{u}} \cdot \nabla)\,T = \nabla^2 T + Q \quad (3)$$

where $\vec{\mathbf{u}}$ is the velocity, P is the dynamic pressure, η is the viscosity, ϵ is the strain rate, Ra is the Rayleigh number, T is the temperature and B and C are the buoyancy number and composition, respectively. $\vec{\mathbf{z}}$ is the unit vector in the vertical direction, t is the time and Q is the internal heating rate. The intrinsic density anomaly of pile materials is represented by the buoyancy number defined as $B = \Delta\rho/(\rho\alpha\Delta T)$, where $\Delta\rho/\rho$ is the intrinsic density anomaly of the pile material compared with the background mantle, α is thermal expansivity and ΔT is temperature difference between the surface and CMB. We define the product of B and C as the effective buoyancy ratio, or B^{eff}. Non-dimensional Rayleigh number (Ra) is defined as $Ra = (\rho_0 g a_0 \Delta T D^3)/(\eta_0\kappa_0)$, where ρ_0, g, α_0, η_0 and κ_0 are the background mantle reference density, the gravitational acceleration, the reference thermal expansivity, the reference viscosity and the reference thermal diffusivity, respectively, and D is the thickness of the mantle.

Most cases are computed in 2D Cartesian geometry using an aspect ratio of 1:1 with 256 × 256 elements, but models with an aspect ratio of 6:1 (for example, with 1536 × 256 elements) are also performed and are found to have little difference compared with square geometry. To solve the conservation equations, we use a modified version of the convection code, Citcom[44], that includes thermochemical convection and composition-dependent rheology. We exclude internal heating for all models in this study, which is more appropriate for our 2D Cartesian models[56]. The initial temperature is 0.5 everywhere with small perturbations. The top and the bottom surface are isothermal with $T = 0$ and $T = 1$, respectively. All boundaries are free-slip. The side boundaries are reflective and insulating.

A ratio tracer method[57] with eight million tracers was used for the advection of the compositional field. On average, each element has 20 randomly distributed tracers which are advected with mantle flow. Initially, a global layer of pile material was introduced to the lowermost mantle, which was later pushed by cold downwellings into a thermochemical pile to the side boundaries of the model domain.

Pile materials are consistently entrained up and mixed into the background mantle, affecting the density of the background mantle. We therefore change pile materials into background mantle materials once they are entrained to the upper mantle. Some background mantle materials are mixed into the thermochemical piles as well, but they do not substantially affect the intrinsic density of the piles. For example, the intrinsic density of the thermochemical pile in the reference case changes by less than 0.3% after ~4.6 Gyr.

Six regional spherical 3D models are computed to compare with 2D results. Equations (1–3) are solved using the CitcomCU code[58], which is available at https://geodynamics.org/cig/software/citcomcu/. The dimension of the computational domain is very close to our 2D case but is in 3D. The domain is divided into 128 × 128 × 128 elements in the horizontal and vertical directions, respectively. To make better comparison with the 2D case, we use the same Rayleigh number and viscosity law as in the 2D models. We first find five representative 2D models with different initial pile volume, pile viscosity, pile buoyancy number and background mantle viscosity. For each 2D model, we construct a corresponding 3D model with the same physical parameters for pile and background mantle materials. For each 3D model, we use an initial temperature that is equal to the steady-state average background mantle temperature in its corresponding 2D model, and we adjust the internal heating rate to make the 3D model have a similar average background mantle temperature as its corresponding 2D model. In addition, we impose a constant westward surface velocity in 3D models, with its value the same as the steady-state average surface velocity in the corresponding 2D models.

The parameters for all cases used in this study are listed in Supplementary Data 1.

Data availability

All seismic tomography models are downloaded from the SubMachine[59] website. The seismic data and all other source data about geodynamic modelling results presented in this study are available at https://figshare.com/projects/Yuan_Li_2022_NG/129185. The seismic data include 17 global shear-wave models, including TX2011[2], GyPSuM-S[15], SAW642ANb[16], SEMUCB-WM1[17], SEMum[18], SGLOBE-rani[19], TX2015[20], SEISGLOB1[21], SEISGLOB2[22], HMSL-S06[23], PRI-S05[24], SP12RTS-S[25], SPani-S[26], S20RTS[27], S362ANI+M[28], S40RTS[29] and SAVANI[30].

Code availability

The author's modified 2D Citcom code used in this study is available from https://figshare.com/projects/Yuan_Li_2022_NG/129185. The CitcomCU code is available at https://geodynamics.org/cig/software/citcomcu/.

References

56. Farrell, K. A. O. & Lowman, J. P. Emulating the thermal structure of spherical shell convection in plane-layer geometry mantle convection models. *Phys. Earth Planet. Inter.* **182**, 73–84 (2010).
57. Tackley, P. J. & King, S. D. Testing the tracer ratio method for modeling active compositional fields in mantle convection simulations. *Geochem. Geophys. Geosyst.* **4**, 8302 (2003).
58. Zhong, S. Constraints on thermochemical convection of the mantle from plume heat flux, plume excess temperature, and upper mantle temperature. *J. Geophys. Res. Solid Earth* **111**, B04409 (2006).
59. Hosseini, K. et al. SubMachine: web-based tools for exploring seismic tomography and other models of Earth's deep interior. *Geochem. Geophys. Geosyst.* **19**, 1464–1483 (2018).

Acknowledgements

We are grateful to the extensive discussions and comments on the manuscript by E. Garnero. We also thank K. Hosseini for SubMachine datasets and Y. Wang and S. Yu for valuable comments. The numerical models were performed on the Agave cluster at Arizona State University. Both Q.Y. and M.L. are supported by National Science Foundation grant numbers EAR-1849949 and EAR-1855624.

Author contributions

M.L. conceived the project and Q.Y. performed all experiments. Both authors analysed the data and wrote the manuscript.

Competing interests

The authors declare no competing interests.

Additional information

Extended data is available for this paper at https://doi.org/10.1038/s41561-022-00908-3.

Supplementary information The online version contains supplementary material available at https://doi.org/10.1038/s41561-022-00908-3.

Correspondence and requests for materials should be addressed to Qian Yuan.

Peer review information *Nature Geoscience* thanks Wei Leng, Neala Creasy and the other, anonymous, reviewer(s) for their contribution to the peer review of this work. Primary Handling Editors: Louise Hawkins and Stefan Lachowycz, in collaboration with the *Nature Geoscience* team.

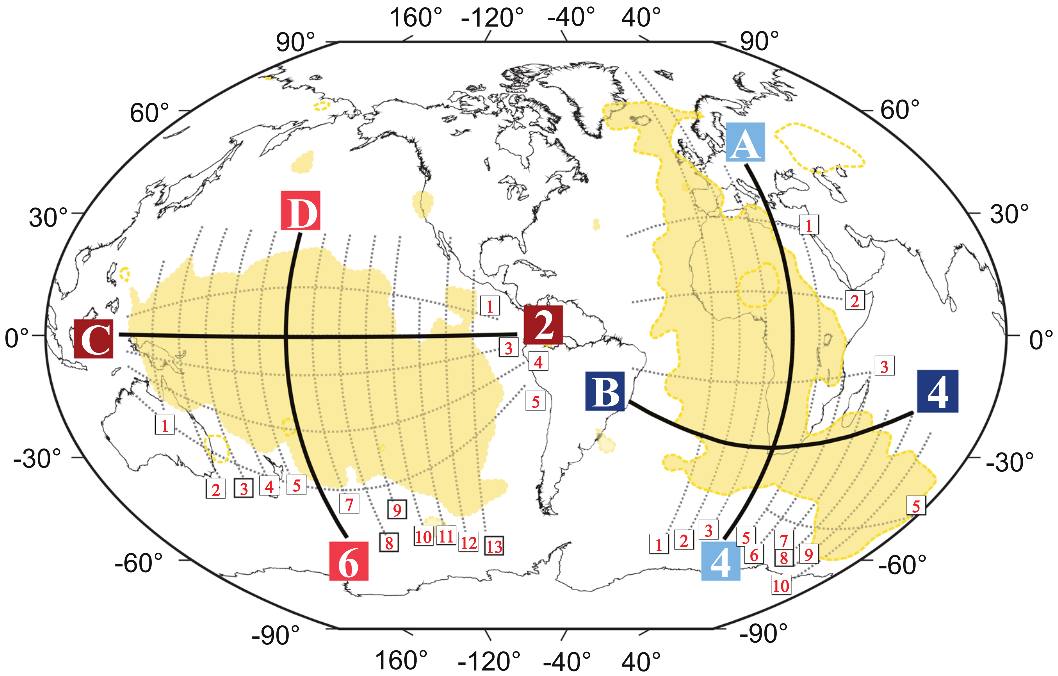

Extended Data Fig. 1 | Cross-section locations through two LLSVPs used for depth profiles of the averaged V_s anomaly. A1-A10 and B1-B5 are for African LLSVP while C1-C5 and D1-D13 performed for Pacific LLSVP. A4, B4 and C2, D6 are the four cross-sections that were found bear the maximum height for African and Pacific LLSVP, respectively. They are respectively named as AA´, BB´ and CC´, DD´ in the main text. All section data are downloaded from the SubMachine website[59]. The 17 global S-wave models are TX2011[2], GyPSuM-S[15], SAW642ANb[16], SEMUCB-WM1[17], SEMum[18], SGLOBE-rani[19], TX2015[20], SEISGLOB1[21], SEISGLOB2[22], HMSL-S06[23], PRI-S05[24], SP12RTS-S[25], SPani-S[26], S20RTS[27], S362ANI + M[28], S40RTS[29], SAVANI[30]. This figure was generated using GMT software version 6.0.0 (https://www.generic-mapping-tools.org/).

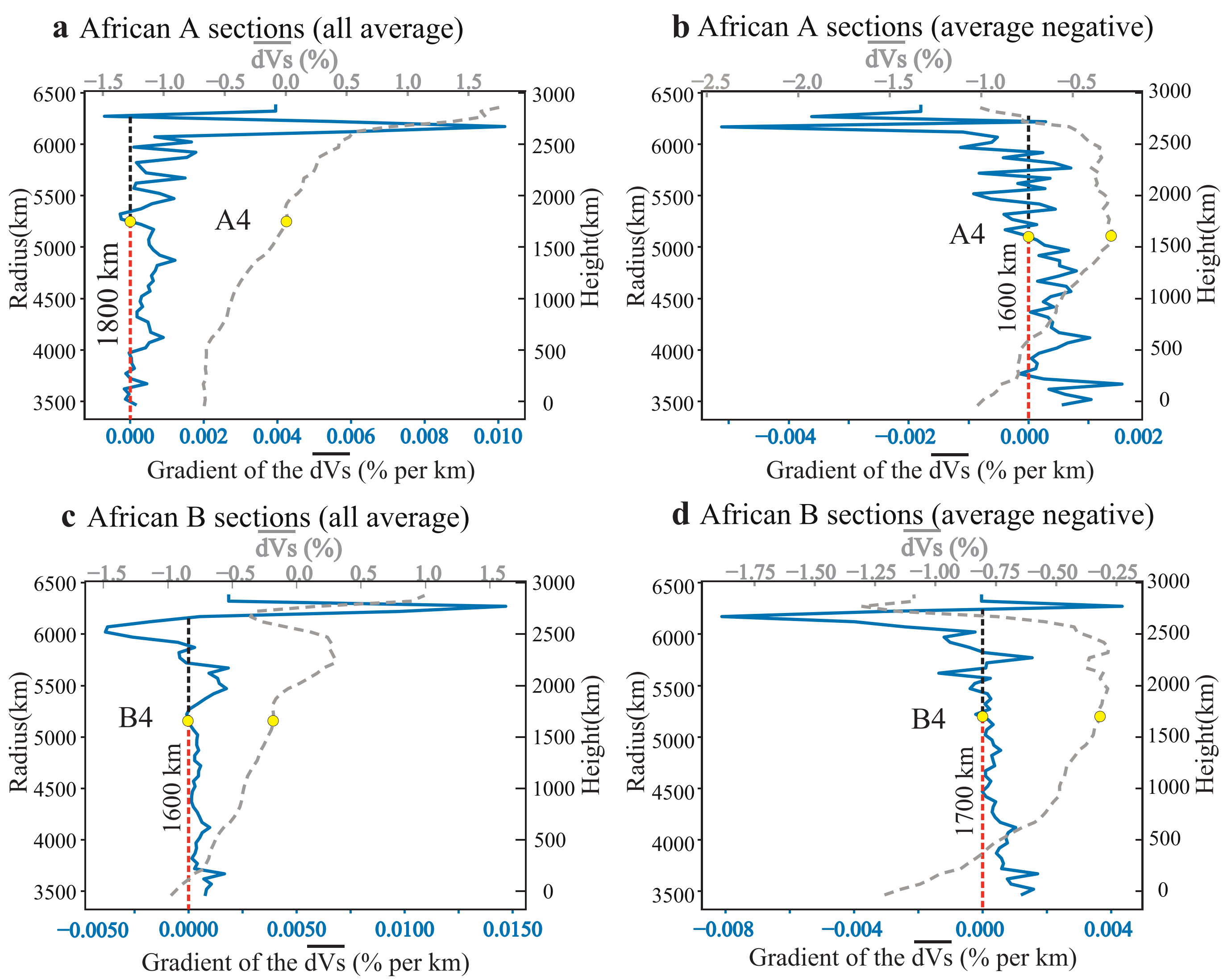

Extended Data Fig. 2 | Depth profiles of the $\overline{dV_s}$ (gray dashed line) and their gradient (blue lines) at 2 selected vertical cross-section locations through the African LLSVP. a, c, the gradient of the $\overline{dV_s}$ as a function of depth for African A4 and B4 vertical cross-sections as shown in Extended Data Fig. 1. **b, d**, similar to panel **a** and **c**, but only the negative values of dV_s are used when calculating the $\overline{dV_s}$. Below the turning point (yellow filled circle) the gradient is mostly positive (shown by the vertical red dotted lines), while above which the gradient is fluctuating around 0 (shown by the vertical black dotted lines). The gradient is defined by the change of $\overline{dV_s}$ over the change of radius.

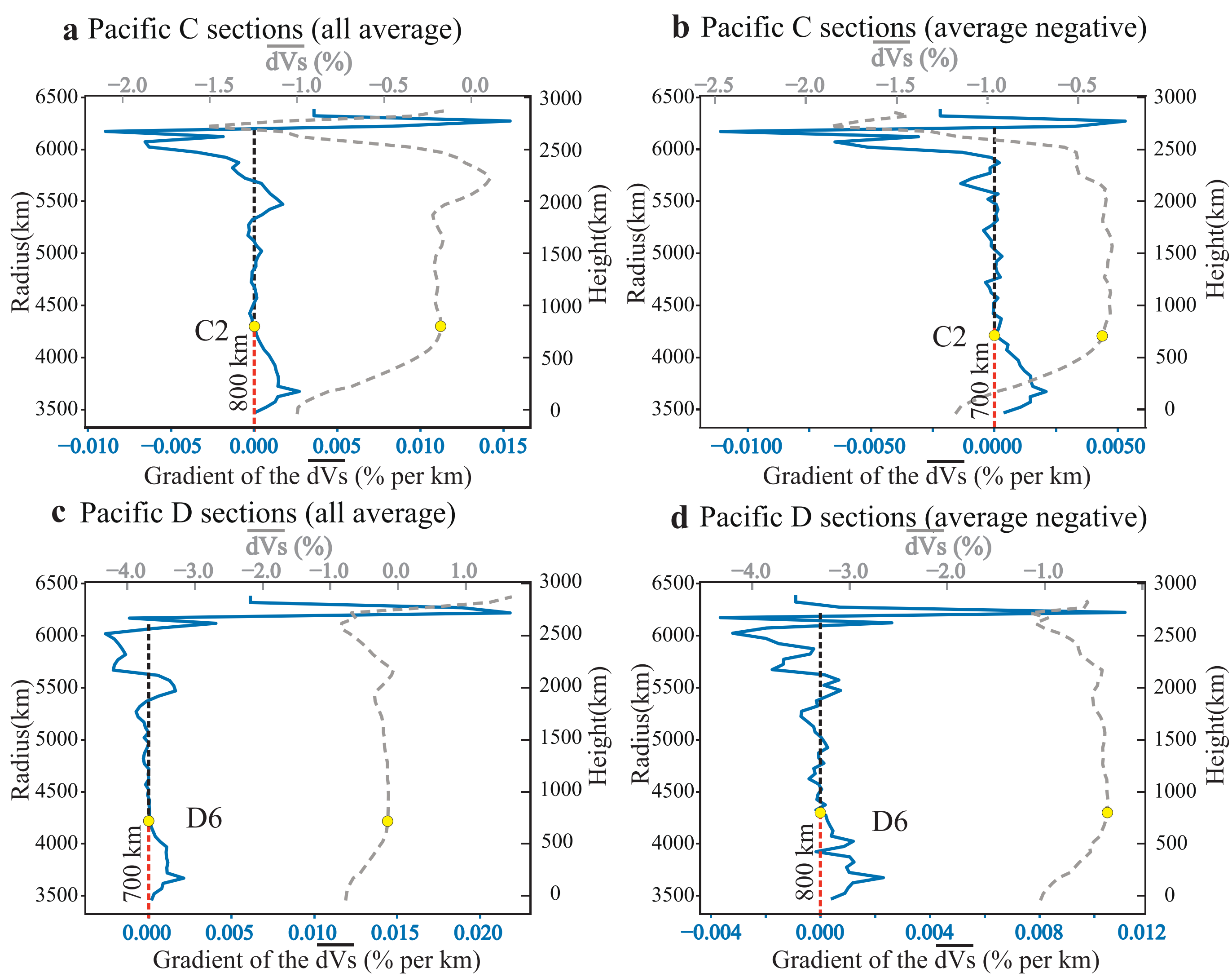

Extended Data Fig. 3 | Depth profiles of the $\overline{dV_s}$ (gray dashed line) and its gradient (blue line) at 2 selected vertical cross-section locations through the Pacific LLSVP. a, c, the gradient of the $\overline{dV_s}$ as a function of depth for Pacific C2 and D6 vertical cross-sections as shown in Extended Data Fig. 1. **b, d**, similar to panel **a** and **c**, but only the negative values of dV_s are used when calculating the $\overline{dV_s}$. Below the turning point (yellow filled circle) the gradients are mostly positive (shown by the vertical red dotted lines), while above which the gradient is fluctuating around 0 (shown by the vertical black dotted lines). The gradient is defined by the change of $\overline{dV_s}$ over the change of radius.

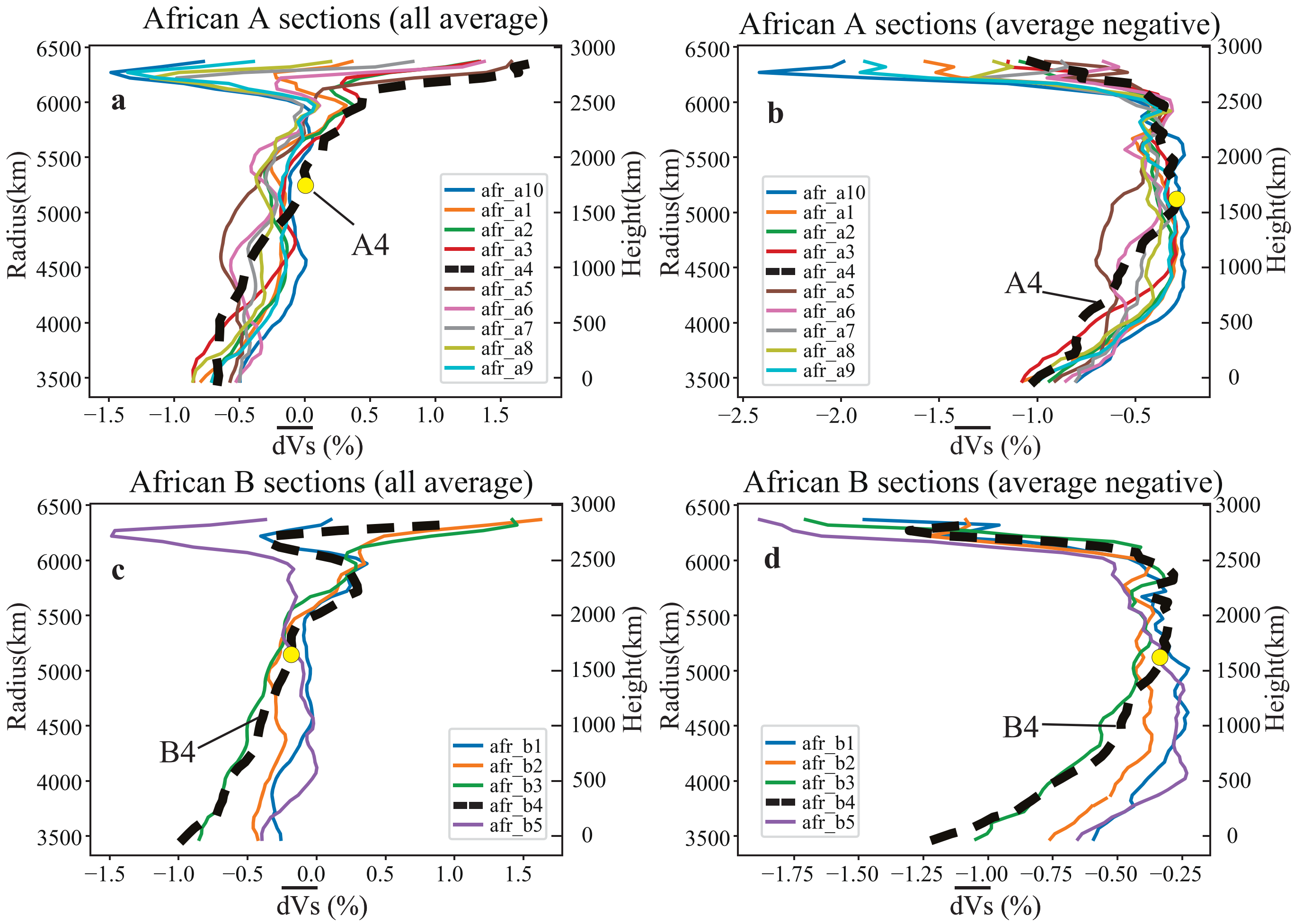

Extended Data Fig. 4 | Depth profiles of the $\overline{dV_s}$ at 15 vertical cross-section locations through the African LLSVP. a, the horizontally averaged $\overline{dV_s}$ as a function of depth for the 10 vertical cross-sections as shown in Extended Data Fig. 1. **b**, similar to panel **a**, but only the negative values of dV_s are used when calculating the $\overline{dV_s}$. **c**, the horizontally averaged $\overline{dV_s}$ as a function of depth for the 5 vertical cross-sections as shown in Extended Data Fig. 1. **d**, similar to panel **c**, but only the negative values of dV_s are used when calculating the $\overline{dV_s}$. The yellow filled circle marks the turning point we defined as the maximum height in main text.

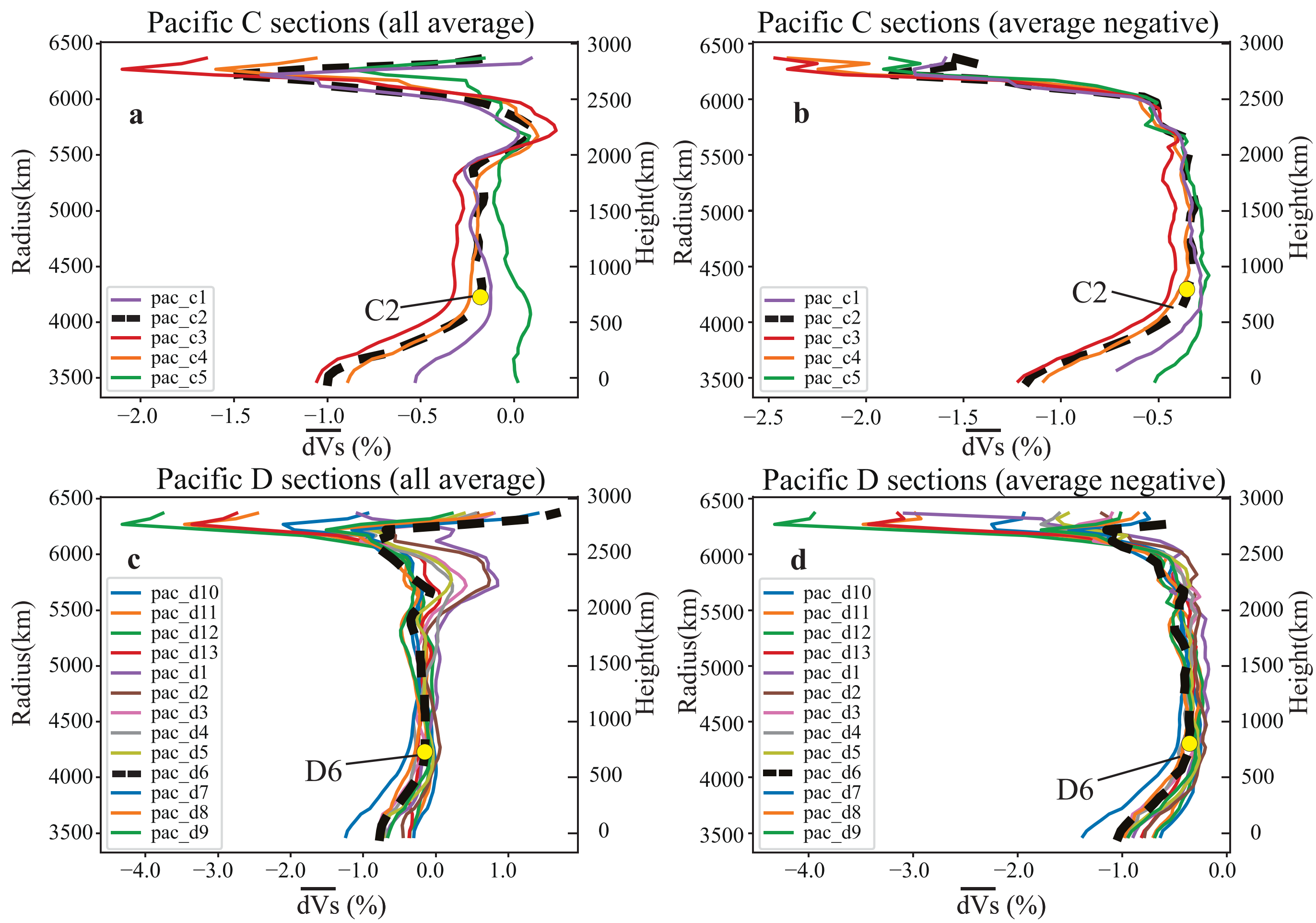

Extended Data Fig. 5 | Depth profiles of the $\overline{dV_s}$ at 18 vertical cross-section locations through the Pacific LLSVP. **a**, the horizontally averaged $\overline{dV_s}$ as a function of depth for the 5 vertical cross-sections as shown in Extended Data Fig. 1. **b**, similar to panel **a**, but only the negative values of dV_s are used when calculating the $\overline{dV_s}$. **c**, the horizontally averaged $\overline{dV_s}$ as a function of depth for the 13 vertical cross-sections as shown in Extended Data Fig. 1. **d**, similar to panel **c**, but only the negative values of dV_s are used when calculating the $\overline{dV_s}$. The yellow filled circle marks the turning point we defined as the maximum height in main text.

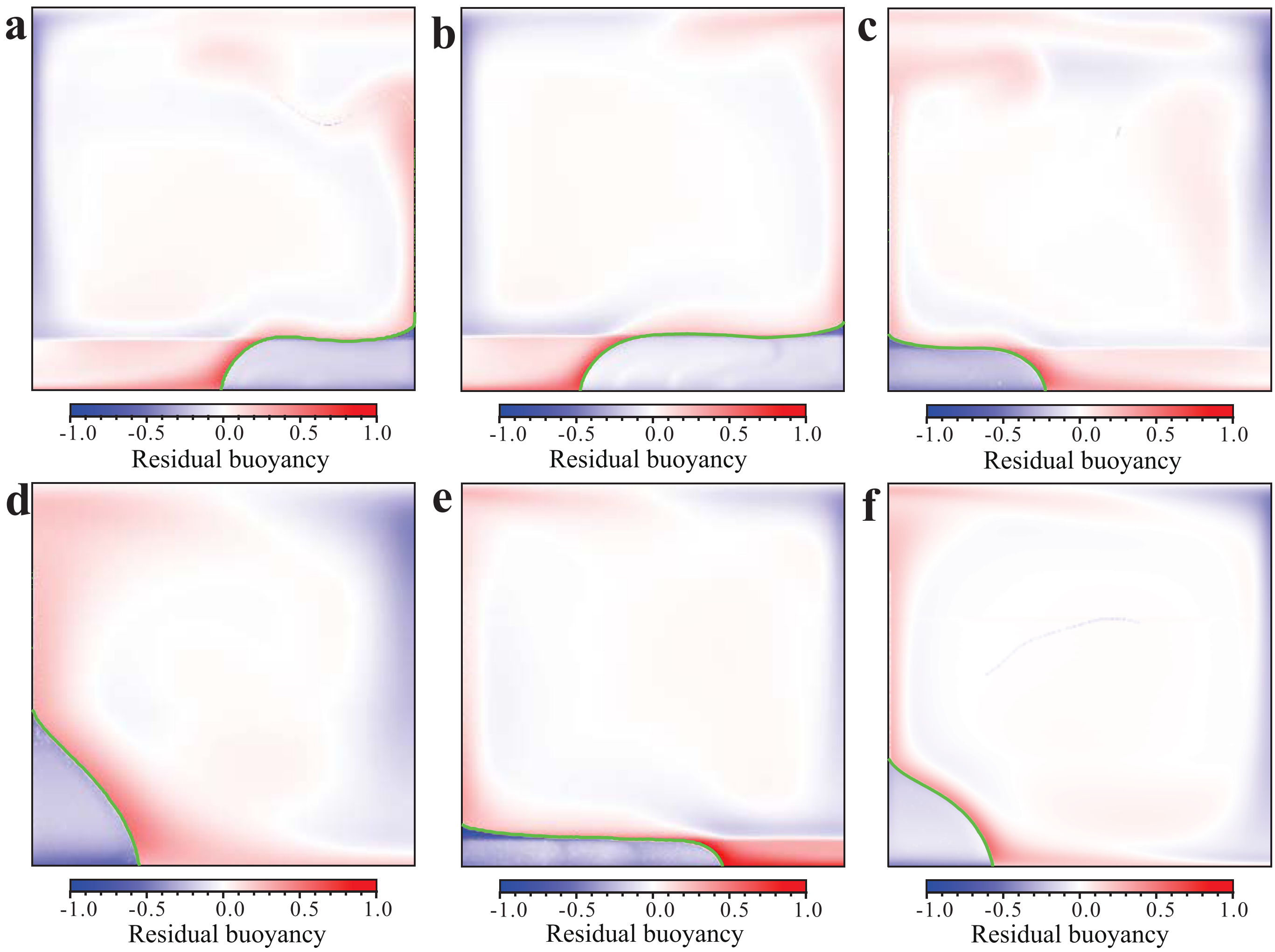

Extended Data Fig. 6 | The effects of model parameters on the height of piles revealed by the field of residual buoyancy (with the horizontal averaged removed). **a**, the reference case. From **b** to **f**, only one parameter is modified from the reference case, they are respectively the initial volume of pile materials (11%) (**b**), pile viscosity (30 times higher than the reference run) (**c**), 25 times higher background mantle viscosity (**d**), a larger buoyancy number of 1.2 (**e**), and smaller buoyancy number of 0.6 (**f**). Green curves show pile edges.

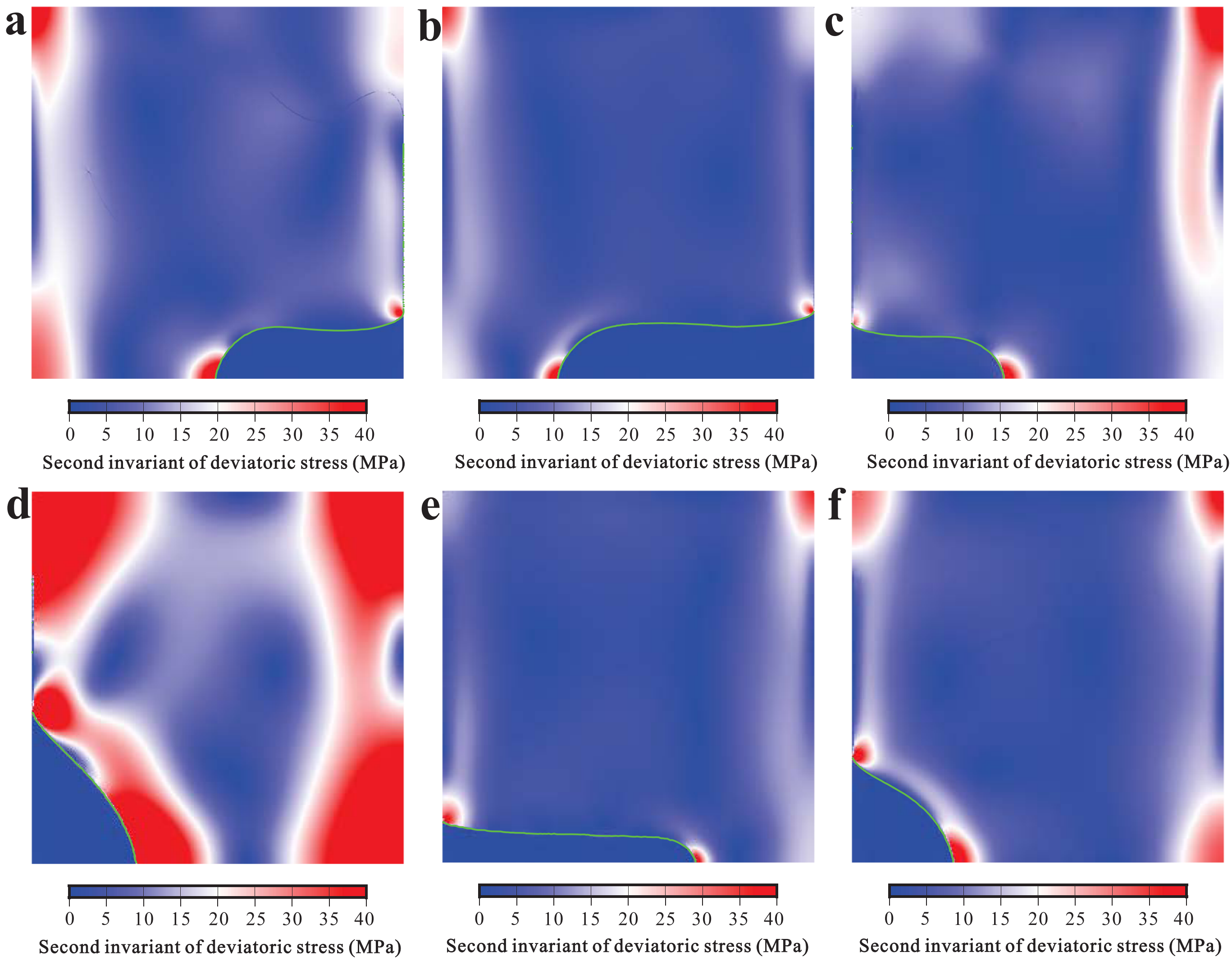

Extended Data Fig. 7 | The effects of model parameters on the height of piles revealed by the deviatoric stress. All cases here from a-f are the same corresponding to that in Extended Data Fig. 6. The green curves show the pile edges.

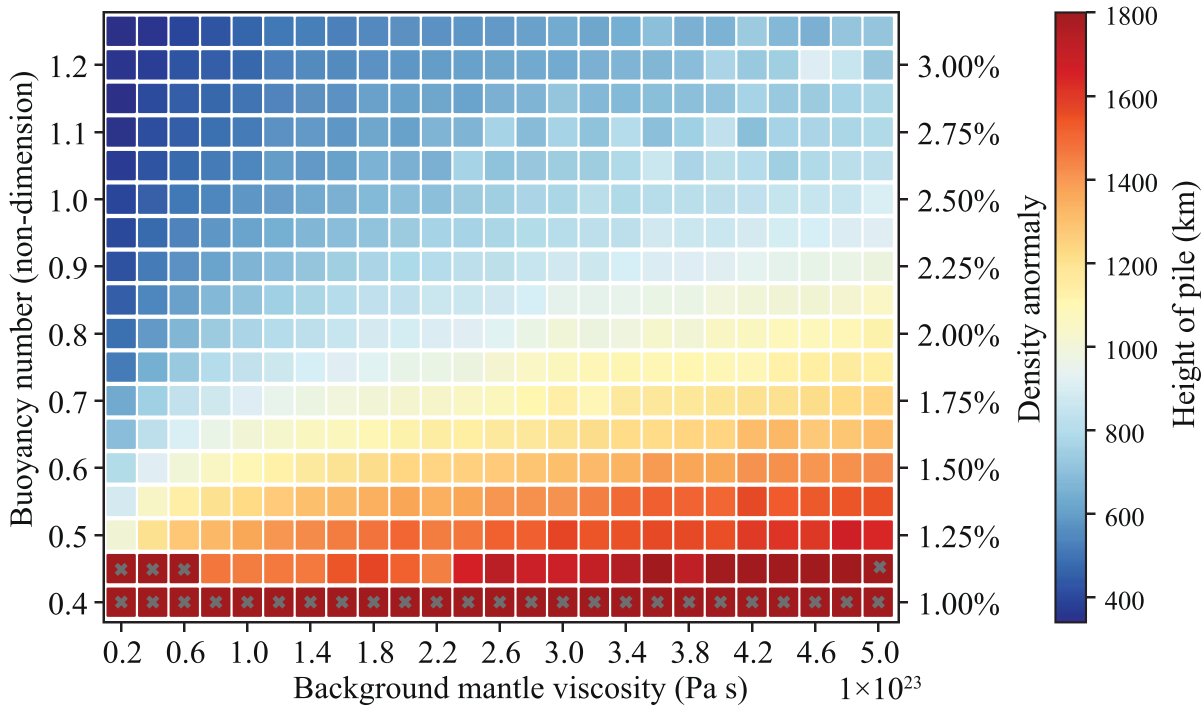

Extended Data Fig. 8 | Pile height as a function of pile buoyancy number and background mantle viscosity for 450 individual models. Gray crosses indicate the cases that the thermochemical piles are not stable.

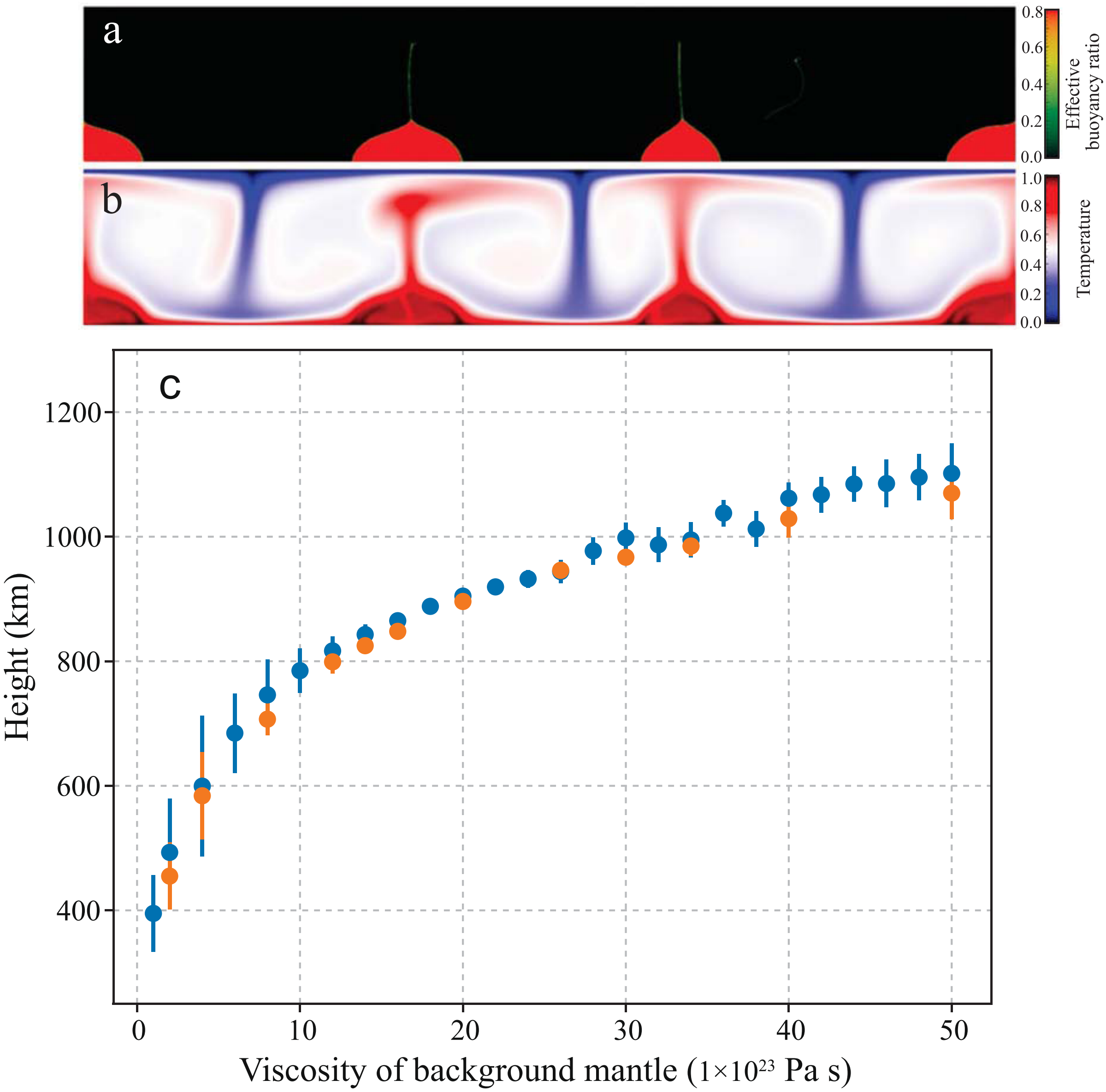

Extended Data Fig. 9 | The effect of different geometry on pile height. a and **b** show the composition and temperature fields respectively for a model of same parameters with the reference case but with aspect ratio of 6. **c**, Blue solid circles show the height of pile from models with aspect ratio of 1, and orange solid circles show the height of pile from models with aspect ratio of 6. The error bar of each calculation refers to one standard deviation of the maximum heights from different timesteps when the model reached steady state. The composition field in panel **a** shows pure background mantle materials ($B^{eff} = 0$), pure pile materials ($B^{eff} = 0.8$), or a mixture between them (intermediate values).

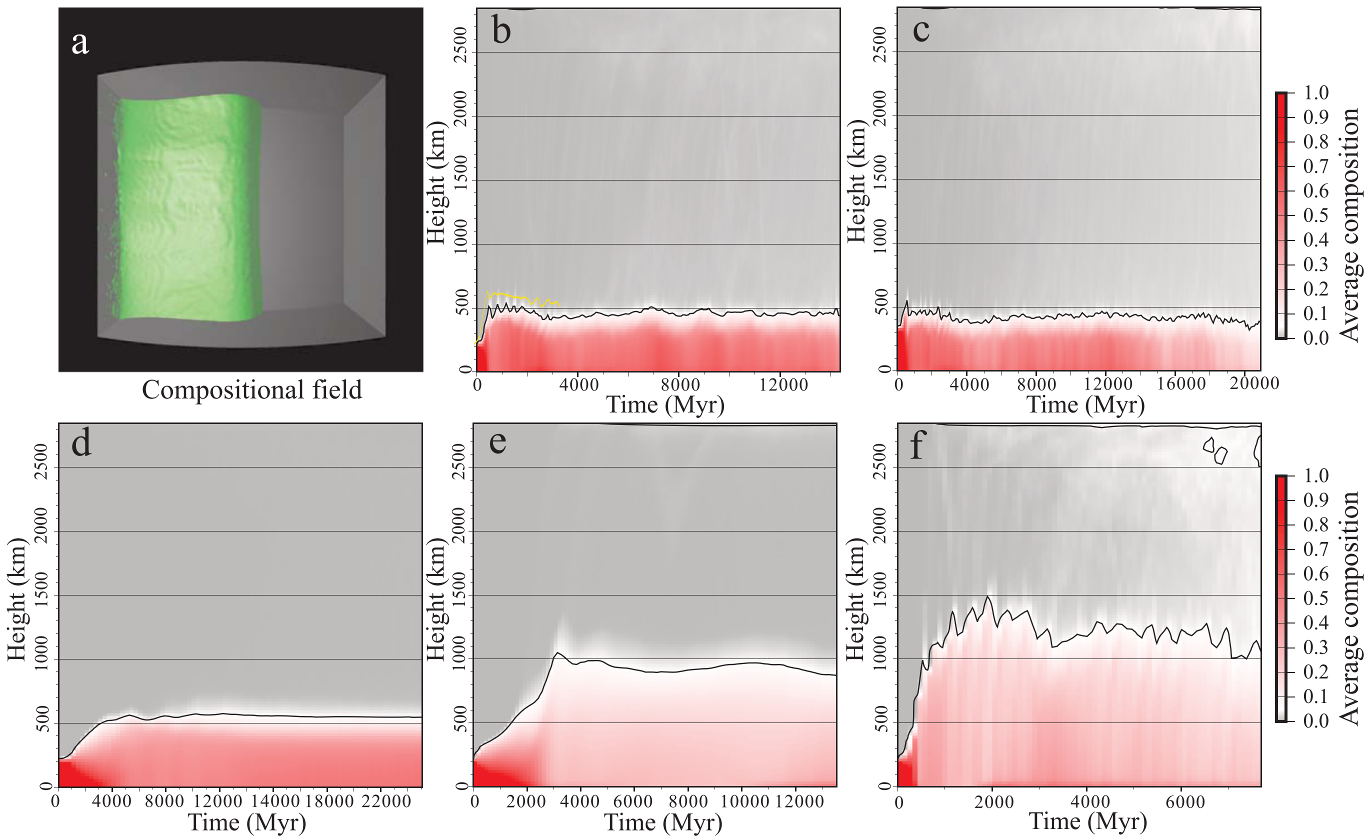

Extended Data Fig. 10 | The setup and height of piles in 3D models. (**a**), snapshot of the compositional field in the 3D reference case whose parameters are the same as the 2D reference case. Only the lowermost 1,000 km of the model domain is shown. (**b-f**), the laterally averaged composition as a function of depth (represented by the height above the CMB) and time for the 3D reference model (**b**), and other 3D models with 4% more initial pile volume (**c**), 100 times higher pile viscosity (**d**), 20 times higher background mantle viscosity (**e**), and a smaller buoyancy number of 0.5 (**f**). The black curves show the contours at average composition of 0.05, which are defined as the top of the thermochemical piles. The yellow curve in (b) are the same contour of a higher resolution case, whose parameters are the same to the 3D reference model.